

Berry paramagnetism in the Dirac semimetal ZrTe_5

Sanghyun Ji ¹, Sang-Eon Lee¹ & Myung-Hwa Jung ¹✉

Dirac matters have attracted a lot of interest due to their unique band structure with linear band dispersions, which have great potential for technological applications. Recently, three-dimensional Dirac and Weyl semimetals have invoked distinctive phenomena originating from a non-trivial Berry phase. In this study, we prepare single crystals of $\text{Ti}_x\text{Zr}_{1-x}\text{Te}_5$ with a highly anisotropic Fermi surface. Our detailed electrical transport measurements reveal that the crystals show the Lifshitz transition, and Ti doping induces a band shift. Further quantum oscillation analyses demonstrate that the $\text{Ti}_x\text{Zr}_{1-x}\text{Te}_5$ crystals are 3D Dirac semimetals. Additionally, we observed a minimum temperature-dependent magnetic susceptibility, which is close to a peak position of electrical resistivity. This observation is interpreted in terms of the Berry paramagnetism. Our finding paves the way to determine a band topology by magnetism and also provides a platform to apply the Berry magnetism to Dirac semimetals.

¹Department of Physics, Sogang University, Seoul 04107, Korea. ✉email: mhjung@sogang.ac.kr

Various phenomena in topological materials, such as the chiral magnetic effect, anomalous Hall effect, and quantum anomalous Hall effect, have attracted attention^{1–5}. A nontrivial π Berry's phase of topological materials plays an important role in the unconventional phenomena. However, magnetic properties associated with a nontrivial π Berry's phase have rarely been reported. The recent studies on Weyl semimetals, such as NbAs and TaAs^{6,7}, show that they can display unconventional paramagnetic and diamagnetic contributions due to the magnetic field-independent 0th Landau level, unlike conventional materials with a parabolic band. The same phenomena can occur in Dirac semimetals (DSMs) if a material has Dirac points in an appropriate position. Landau levels under magnetic field depend on a relative angle between the magnetic field direction and the line connecting the Dirac points⁶. Therefore, Berry paramagnetism in DSMs is usually complex; there are just a few examples of an application of the Berry paramagnetism to DSMs⁸. Hence, prominent experimental evidence can be obtained in DSMs with a single Dirac cone.

Zirconium pentatelluride, ZrTe_5 , has recently been proposed as 3D DSMs with a Dirac cone at Γ point located at the phase boundary between weak and strong topological insulators^{9,10}. More recent studies have shown that ZrTe_5 exerts a topological phase transition due to external parameters such as pressure, strain, and photoexcitation^{11–14}. The resistivity shows the maximum value at finite temperature, often called resistivity anomaly, which is the hallmark property of ZrTe_5 . The anomaly is interpreted as a result of carrier-type transition accompanied by a band shift with temperature^{15,16}. However, there is another interpretation that the anomaly comes from a topological phase transition by gap opening^{8,17}. A peak temperature of resistivity is indicative of charge-neutral point, Dirac point, and is observed differently depending on the growth method and growth condition^{2,4,8,18}. Hence, most studies have been devoted to verifying topological characteristics by measuring transport and spectroscopic properties, such as magnetoresistance (MR) and angle-resolved photoemission spectroscopy^{13,15,19–21}.

This study highlights band topology in DSMs in magnetic data, interpreted as the Berry paramagnetism. A similar scheme has been applied in ZrTe_5 ⁸; however, our crystals show different properties (Supplementary Note 1). We prepared single crystals of $\text{Ti}_x\text{Zr}_{1-x}\text{Te}_5$ ($x=0, 0.1, \text{ and } 0.2$) using a chemical vapor transport method. We observed quasi-2D transport due to its highly anisotropic nature of the Fermi surface and the resistivity peak at $T_p = 122$ K due to temperature-induced band shift, i.e., Lifshitz transition. This result is compared to the previous work by Nair et al.⁸. They reported the resistivity peak at 34 K due to topological phase transition rather than Lifshitz transition.

As x increases, where Zr is replaced by an isovalent Ti with a smaller radius, we observed that lattice constant is reduced along the b axis, van der Waals interlayer spacing. Thereby, T_p decreases to 92 and 85 K for $x=0.1$ and 0.2 , respectively. Transport measurements showed that the isovalent substitution induces the band shift without significantly modifying the anisotropic Fermi surface. Furthermore, quantum oscillation analyses showed that our $\text{Ti}_x\text{Zr}_{1-x}\text{Te}_5$ crystals are 3D DSMs with a nontrivial π Berry phase and an additional phase shift of $1/8$. In further studies on magnetic properties of ZrTe_5 , a minimum value of magnetization was observed at finite temperature, T_m , with strong anisotropy. Although such temperature-dependent magnetization was reported^{22,23}, its origin has still been puzzling. We found that T_m coincides with T_p for all x . Moreover, magnetization is most prominent when a magnetic field is applied along the b axis, where the effective cyclotron mass is the smallest. The resistivity and magnetization curves are well-scaled into a single curve, implying that a single mechanism dominates both

phenomena. Finally, based on the Berry paramagnetism picture, we simulated the experimentally measured magnetization data using the band parameters obtained in this study. It was in good agreement with the magnetization results, including the quantum oscillations. Our study revealed that the strongly temperature-dependent magnetization of ZrTe_5 originates from its topological character. Since ZrTe_5 is a DSM whose band sensitively shifts by temperature, it is a suitable example to apply the Berry paramagnetism.

Results and discussion

Reduced lattice parameter b by Ti substitution. Single crystals of pristine and Ti-substituted ZrTe_5 were grown by a chemical vapor transport method. Figure 1a displays the single-crystal X-ray diffraction (XRD) patterns for $\text{Ti}_x\text{Zr}_{1-x}\text{Te}_5$ ($x=0, 0.1, \text{ and } 0.2$). The shiny surface of each crystal was set to be the diffraction plane due to the needle-like shape of crystals with a large shiny surface (Fig. 1b). The XRD patterns were indexed to the orthorhombic layered structure with space group $Cmcm$. Figure 1c shows that the prism chains of ZrTe_3 are along the a axis (which corresponds to the elongated direction of the needle-shaped crystal). These chains are bonded via zigzag Te atoms along the c axis to form a sheet of ZrTe_5 in the ac plane (which corresponds to the shiny surface of the crystal), and the ZrTe_5 sheets are stacked along the b axis with weak van der Waals interaction. Hence, the single crystals are well cleaved along the b direction. The XRD peaks of the cleaved ac plane show the $(0k0)$ peaks of ZrTe_5 . The evaluated lattice parameter of b is $14.52(3)$ Å for $x=0$, which agrees with the previously reported value¹⁴. As x increases, the lattice parameter decreases to $14.51(4)$ Å for $x=0.1$ and $14.47(2)$ Å for $x=0.2$ (Fig. 1d). In addition, the lattice parameter b is expected to be most affected by the substitution due to weak van der Waals bonding. The relative changes of the other lattice parameters were investigated using scanning tunneling microscopy (STM). The representative STM image performed on the cleaved ac surface for $x=0.1$ is plotted in Fig. 1e. We observed bright stripes parallel to the a axis, as evidenced by the chain structure of ZrTe_3 . The separation of chains is ~ 13.8 Å, which matches the lattice parameter c of pristine ZrTe_5 ¹⁴. In addition, we observed bright and dark spots corresponding to the substituted Ti atoms and Te vacancies, respectively (see Fig. 1e). Considering these results and the fact that the isovalent Ti atoms are replaced by Zr, the topological properties of ZrTe_5 can be mostly governed by the volume change depending on the b lattice parameter, that is, the interlayer spacing, without significant changes in the band structure.

Effect of Ti substitution on transport properties. To investigate changes in the band structure by the Ti substitution, we first began with transport results of Hall resistivity, ρ_{xy} , with varying temperatures (Fig. 2a–c). A current was fixed to flow along the a axis, and a magnetic field was applied to the b axis. For $x=0$, the slope of ρ_{xy} was negative at low temperatures, while it was positive at high temperatures. This indicates that dominant charge carriers are electrons at low temperatures and holes at high temperatures. Since the ρ_{xy} curves are not linear to the magnetic field, we analyzed the data by the two-carrier model. The electrical resistivities, ρ_{xx} and ρ_{xy} were converted into the conductivities, σ_{xx} and σ_{xy} (Supplementary Note 2) for precise analyses, which allow calculating carrier density, n , and carrier mobility μ . We noted one carrier with higher mobility as carrier 1 and the other carrier with lower mobility as carrier 2. The temperature dependence of n and μ of the two carriers is plotted in Fig. 2d–f and g–i, respectively. For $x=0$, the dominant electron density of $n_1 = 4.3 \times 10^{17} \text{ cm}^{-3}$ at 2 K exhibits an ultrahigh mobility of

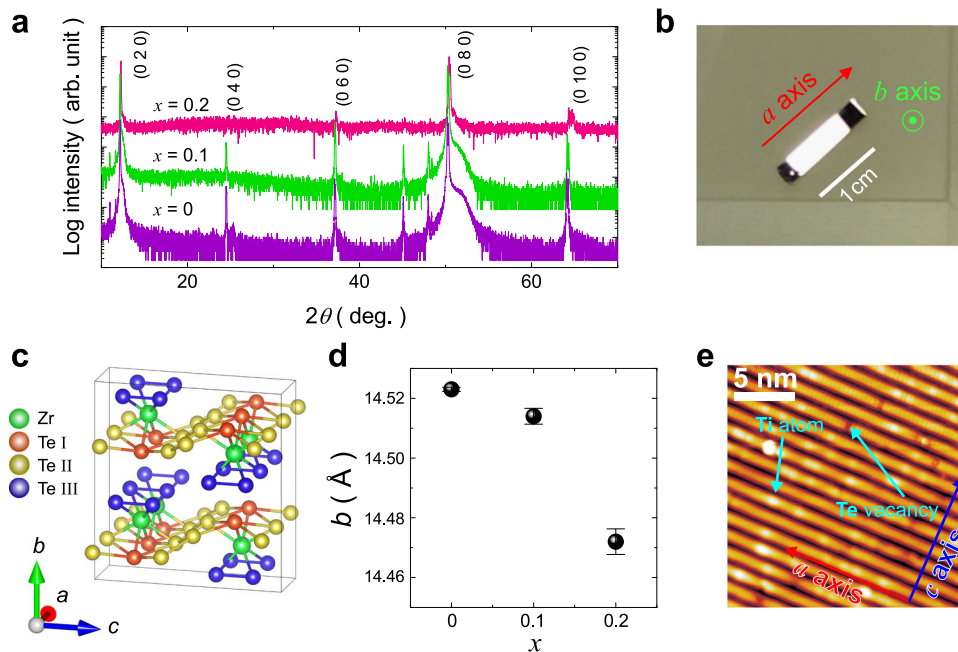


Fig. 1 Material characterization of pristine and Ti-doped ZrTe_5 . **a** X-ray diffraction patterns of single crystals. All peaks correspond to the $(0k0)$ plane. **b** Micro-optics image of a typical single crystal. The single crystals naturally grow along the a axis. **c** The crystal structure of ZrTe_5 . The van der Waal bonding is along the b axis. **d** Estimated lattice constant of b . The error bars represent the standard errors of the linear fit of Bragg's law. **e** Scanning tunneling microscopy image of $x = 0.1$ crystal as a representative. Clear stripe patterns are shown in the ac plane.

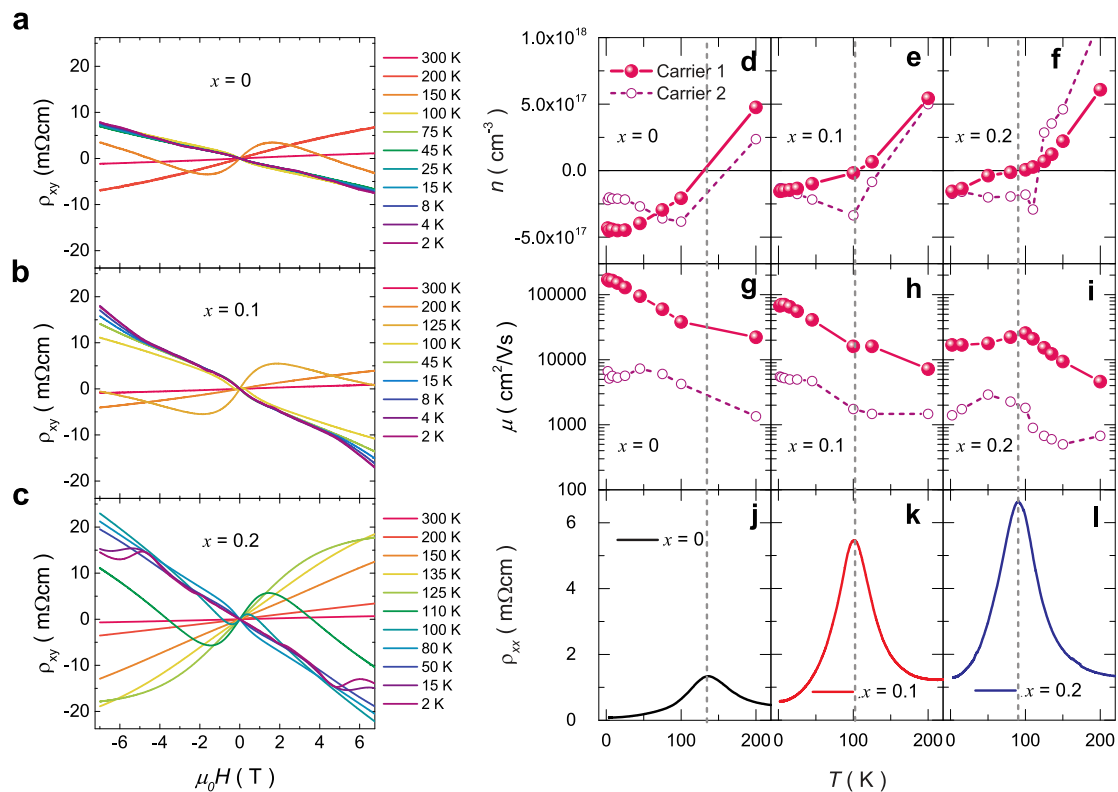


Fig. 2 Transport properties of $\text{Ti}_x\text{Zr}_{1-x}\text{Te}_5$. **a-c** Hall resistivity as a function of a magnetic field. **d-f** Carrier density and **g-i** carrier mobility as a function of temperature evaluated by the two-carrier model. The error bars of **d-i** are the standard errors of the two band fit, which are smaller than the size of the data symbols. **j-l** Electrical resistivity as a function of temperature. The gray lines are drawn as a guide for T_{pr} , the temperature showing the resistivity peak.

$\sim\mu_1 = 170,000 \text{ cm}^2 \text{ V}^{-1} \text{ s}^{-1}$. It is much larger than the previously reported typical value ($\sim 50,000 \text{ cm}^2 \text{ V}^{-1} \text{ s}^{-1}$)²⁴, indicating the high quality of our single crystals. As temperature increases, the carrier mobility decreases to approximately one-tenth of the value at low temperatures. Moreover, the electron density also decreases; hence, the hole becomes the dominant carrier at high temperatures. The transition of electron-dominant to hole-dominant phases is observed around $T_p = 122 \text{ K}$, where the resistivity shows a peak (Fig. 2j–l). This resistivity peak has also been reported in typical ZrTe_5 samples and has been proposed to be indicative of a charge-neutral point, i.e., Dirac point^{15,20,24,25}. Such temperature dependence of ρ_{xx} is evidence of temperature-induced Lifshitz transition¹⁵, describing band shift upward crossing a Dirac point with increasing temperature. As x increases, the overall temperature-dependent behavior is similar but tends to shift to a lower temperature. At 2 K, the carrier mobility decreases from $\mu_1 = 170,000 \text{ cm}^2 \text{ V}^{-1} \text{ s}^{-1}$ for $x = 0$ to $67,500 \text{ cm}^2 \text{ V}^{-1} \text{ s}^{-1}$ for $x = 0.1$ and to $16,900 \text{ cm}^2 \text{ V}^{-1} \text{ s}^{-1}$ for $x = 0.2$. According to the relation, $\mu = e\tau_{tr}/m^*$, it is expected that the transport lifetime, τ_{tr} , would decrease or the effective mass, m^* , would increase. We note that the carrier density at 2 K decreases with increasing x , though Ti has an equivalent valence to Zr. Consequently, the electron-dominant to hole-dominant transition moves to a lower temperature ($T_p = 92$ and 85 K for $x = 0.1$ and 0.2 , respectively). This result implies that the Ti substitution causes a band shift. Considering that Ti is isovalent to Zr with a smaller atomic radius, the band shift is expected due to the change of the lattice parameter, i.e., interlayer distance.

A Fermi surface topology can be examined by measuring an angle-dependent transport of MR (see Fig. 3a–c). A current was applied along the a axis, and a magnetic field was rotated from the b axis ($\theta = 0^\circ$) to the a axis ($\theta = 90^\circ$). The MR value at 2 K for $x = 0$ reaches up to 2400% with the large peak-like structure at 8 T, agreeing with the previously reported value^{21,24}. The magnitude of MR is strongly suppressed with increasing θ , indicating that the Fermi surface is highly anisotropic. Such

strong suppression is also observed in $x = 0.1$ and 0.2 with a lower MR ratio. As x increases, the MR curves are altered in peak positions as well as magnitudes. The peak position decreases to 5 T for $x = 0.1$ and to 4 T for $x = 0.2$, and the maximum MR magnitude also decreases to 580% for $x = 0.1$ and to 370% for $x = 0.2$. All the MR curves show oscillatory signals with a nonlinear positive background. Oscillatory components, ΔR , of the Shubnikov–de Haas (SdH) effect were extracted by removing backgrounds obtained by averaging the upper and lower envelopes of curves (see Fig. 3d–f). After that, the peak positions were assigned to an integer Landau index N , constructing the Landau fan diagram (Fig. 3g–i). Here, it is noticeable that a single oscillation frequency is observed in the SdH oscillations, although there are two different carriers observed in the Hall results. This result implies that one of the two carriers contributes to the quantum oscillations, which is likely to be the one (carrier 1) with higher mobility.

According to the Lifshitz–Onsager quantization rule, $F/\mu_0 H = N + \gamma$, we obtained the oscillation frequency, F , and the phase, γ , from the slope and the intercept of the linear fit of the Landau fan diagram, respectively. As x increases, the slope gradually decreases; $F = 4.98$ ($x = 0$), 3.64 T ($x = 0.1$), and 3.03 T ($x = 0.2$) at $\theta = 0^\circ$, indicating that the Fermi surface shrinks because an oscillation frequency is proportional to a cross-sectional area of a Fermi surface perpendicular to a magnetic field direction. This result is consistent with that of the Hall measurements in which the dominant carriers move to the hole type by the Ti substitution. In Fig. 3j–l, we plot the results of F and γ versus θ at 2 K. We found that F increases with $1/\cos\theta$, which deviates as θ approaches 90° . This can be understood by the highly anisotropic Fermi surface of ZrTe_5 , as reported earlier^{21,24}. In addition, γ is defined as $\gamma = \frac{1}{2} - \frac{\phi_B}{2\pi} \pm \delta$, where ϕ_B denotes the Berry phase and δ represents an additional phase taken as $\pm 1/8$ or 0 for 3D or 2D Dirac systems, respectively. Our results in most angles show $\gamma \sim 1/8$ (Fig. 3m–o), suggesting that ZrTe_5 is a 3D Dirac system ($\delta = 1/8$) with a nontrivial Berry phase

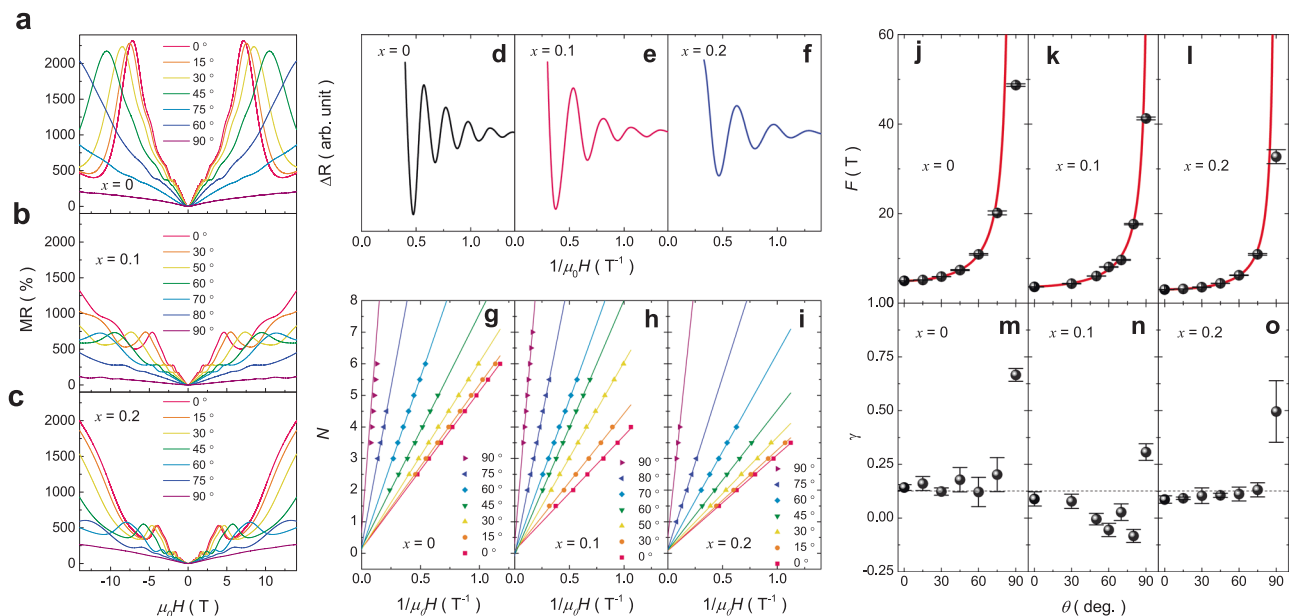


Fig. 3 Angle-dependent magnetoresistance, Shubnikov–de Haas oscillation frequency, and intercept. The magnetic field is swept from the b axis ($\theta = 0^\circ$) to the a axis ($\theta = 90^\circ$) while current flows along the a axis. **a–c** Angle-dependent magnetoresistance ratio as a function of a magnetic field. **d–f** Oscillating components of the magnetoresistance as a function of the inverse magnetic field. **g–i** Landau fan diagram constructed with oscillation components of **d–f**. The inverse magnetic field of the oscillation peaks and valleys are assigned to integer and half-integer, respectively. **j–l** Angle-dependent oscillation frequency, while the red line is $1/\cos\theta$. **m–o** Landau fan diagram intercepts as a function of angle. The dashed line indicates $\gamma = 1/8$. The error bars in **j–o** are the standard errors of the Landau fan diagram fits.

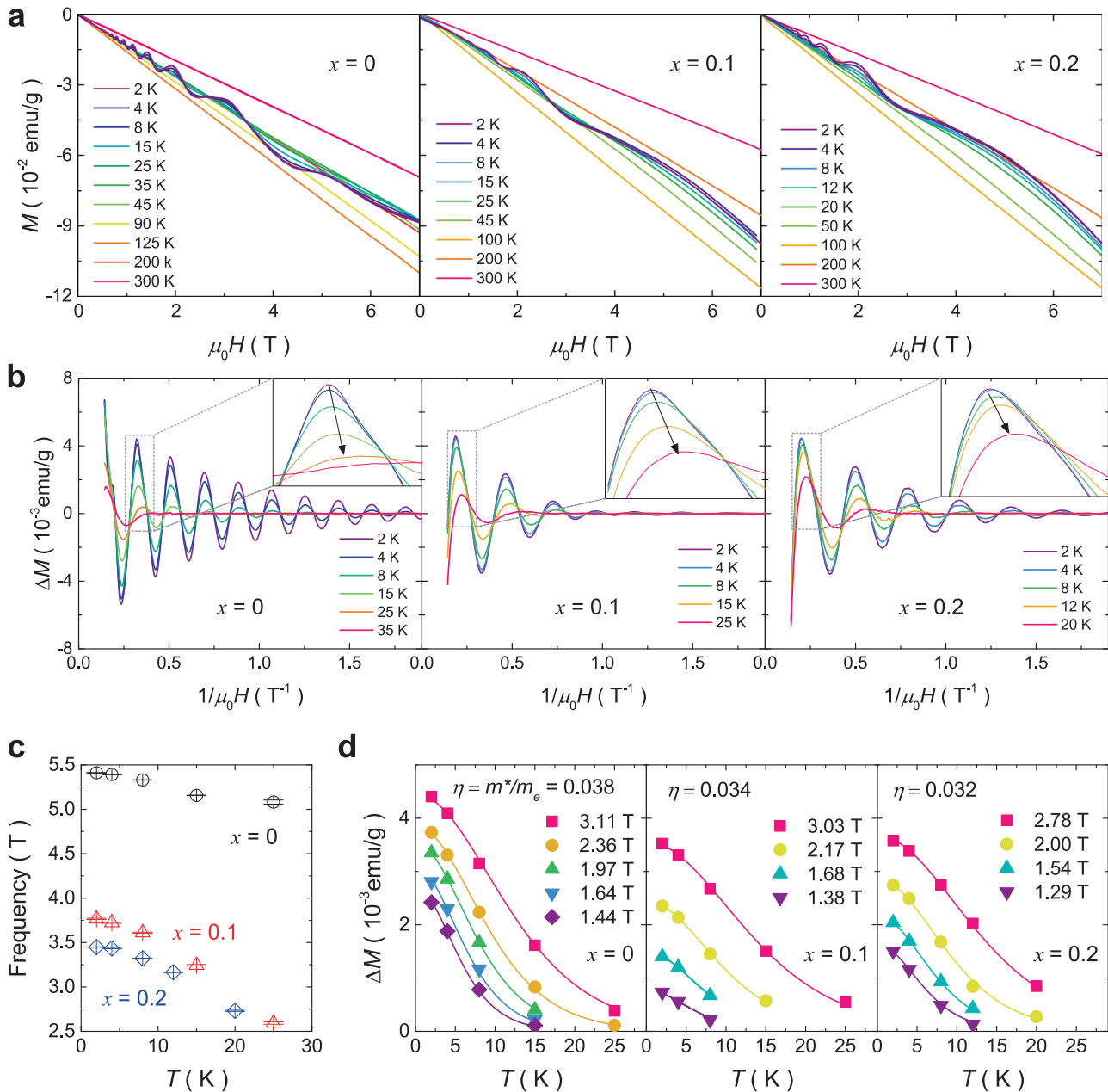


Fig. 4 Magnetization curves of three samples with a magnetic field along the b axis. **a** Raw data of magnetization at various temperatures. **b** Oscillating component of each magnetization with subtracting smooth background in raw data. Magnified single peaks are plotted to show the change of peak position clearly (inset). **c** Temperature-dependent quantum oscillation frequency. The error bars are the standard error of the Lifshitz-Kosevich formula fit. **d** The fit of the temperature reduction factor of quantum oscillations. The effective mass is the global parameter for fitting the amplitudes at different magnetic fields. The evaluated effective mass ratio, $\eta = m^*/m$, of the samples decreases with increasing x . The standard errors of the fits are provided as the error bars of the effective mass ratio.

($\phi_B = \pi$). On the contrary, the deviation at $\theta = 90^\circ$ was observed as a result of the spin zero effect due to the highly anisotropic Fermi surface²⁵. The overall results from the F and γ analyses suggest that the isovalent substitution of Ti for Zr does not significantly modify the anisotropic Fermi surface but simply causes the band shift for the investigated compositions of $x = 0.1$ and 0.2 .

Magnetic properties correlated with the transport properties.

To further characterize the quantum oscillations, we then investigated a field dependence of magnetization $M(H)$. Figure 4a shows $M(H)$ curves measured at different temperatures from 2 to 300 K. $M(H)$ curves show diamagnetic signals at all temperatures

for all samples. Since the diamagnetic signal is the largest when a magnetic field is applied along the b axis (Supplementary Note 3), we plot the $M(H)$ curves representatively for $H//b$ in Fig. 4a. The diamagnetic signal does not monotonically depend on the temperature, which is discussed in more detail later. By subtracting a linear diamagnetic background, we extracted a clear oscillation component, ΔM , of the de Haas van Alphen (dHvA) effect (see Fig. 4b). Note that dHvA oscillations are observable only for $H//b$. The positions of peaks and valleys move to a lower magnetic field with increasing temperature (insets of Fig. 4b). Such an oscillation profile provides evidence of band shift upward, crossing the Dirac point with increasing temperature. Consequently, the oscillation

frequency decreases from $F = 5.4$ T at 2 K to $F = 5.1$ T at 25 K for $x = 0$ (Fig. 4c). In addition, since the Fermi surface shrinks with the Ti substitution, the frequencies for $x = 0.1$ and 0.2 start at lower values; however, similar behavior is observed. The oscillation frequency of $F = 5.4$ T for $x = 0$ decreases to $F = 3.8$ T and to 3.4 T for $x = 0.1$ and $x = 0.2$, respectively, which are in good agreement with the results obtained from the SdH oscillations.

The temperature-dependent ΔM of the dHvA oscillations was fitted with the standard Lifshitz–Kosevich formula, as shown in Fig. 4d. The peak position was corrected to the field value at 2 K. A fit for $x = 0$ yielded an effective cyclotron mass of $m_c = 0.038 m_e$ and a quantum lifetime of $\tau_q = 0.13$ ps, comparable to the previously reported values^{24,25}. As x increases, m_c is slightly reduced to $0.034 m_e$ and to $0.032 m_e$ for $x = 0.1$ and 0.2 , respectively, whereas τ_q is markedly reduced to 0.048 ps and to 0.086 ps for $x = 0.1$ and 0.2 , respectively. The slight reduction of m_c is associated with the shrink of the Fermi surface by the Ti substitution because of the linear relation between m_c and k_F (Supplementary Note 4). We assumed that the Fermi velocity was not significantly altered by the isovalent Ti substitution. Since the change in m_c is small, the aforementioned drastic reduction of μ obtained from the Hall analyses is interpreted due to the decrease in τ_{tr} . The prominent reduction of both τ_q and τ_{tr} can be attributed to more scattering events by substituted Ti atoms. In topological materials or low-dimensional systems, τ_q is frequently compared to τ_{tr} evaluated from Hall effect and resistivity measurements. Note that τ_{tr} is a measure of the motion of charged particles along the electric field gradient, while τ_q denotes the mean time that a carrier remains in a particular state before being scattered to a different state. Moreover, τ_{tr}/τ_q was observed to have a large value because τ_{tr} can overweight large scattering angles over small angle^{26–29}. Indeed, in our quasi-2D material of $\text{Ti}_x\text{Zr}_{1-x}\text{Te}_5$, τ_{tr}/τ_q value was evaluated to be 28 for $x = 0$ and decreases to 3.6 for $x = 0.2$ (Supplementary Note 5).

An interesting feature was found in the temperature dependence of magnetization $\chi(T)$. In Fig. 5a, we plot the $\chi(T)$ data measured in an applied magnetic field of 7 T for three crystal axes. As observed in $M(H)$, diamagnetic signals are clear for all directions in all samples. When a field is applied along the b axis, where an effective cyclotron mass is the smallest (Supplementary Note 4), the diamagnetic signal is the largest with pronounced temperature dependence. Although there are reports showing strongly temperature-dependent magnetization with strong magnetic anisotropy in a pristine ZrTe_5 , its origin is not clear^{22,23}. It is noteworthy that the temperature T_m of $\chi(T)$ minimum is close to the temperature T_p of the ρ_{xx} peak. From this result, we speculate that the mobile carriers mainly governing the transport properties contribute to the magnetic properties. In Fig. 5b, we plot $|n|^{1/3}$ for carrier 1 and carrier 2 as a function of temperature. Since n is proportional to k_F^3 and k_F is proportional to E_F when a band dispersion is linear, $n^{1/3}$ corresponds to E_F . Therefore, $|n|^{1/3}$ indicates a relative position of E_F from a Dirac energy level. It is evident from Fig. 5b that carrier 1 follows the $\chi(T)$ curve for all samples, suggesting that an E_F position is a key parameter to determine the magnetism of $\text{Ti}_x\text{Zr}_{1-x}\text{Te}_5$. In order to verify this close relation between the transport and magnetic properties, the ρ_{xx} and $\chi(T)$ data are plotted as a function of the relative temperatures of $T - T_m$ and $T - T_p$ in Fig. 5c, d, respectively. As aforementioned, the resistivity peak presents the Dirac point so that as E_F moves away from the Dirac point, not only the susceptibility increases but also the resistivity decreases.

Figure 5e summarizes the key observations of $\text{Ti}_x\text{Zr}_{1-x}\text{Te}_5$ by the Ti substitution as well as temperature. First, we observed band shift with increasing temperature; E_F changes while crossing Dirac point from n -type regime to p -type regime. Next, we found band shift with increasing x ; since E_F is closer to the Dirac point

for a larger x , E_F reaches the Dirac point at a lower temperature. Recent studies on Weyl semimetals have reported that a topological nature of Weyl electrons can provide peculiar magnetic responses; nontrivial fermions in states above Weyl nodes contribute to paramagnetism, while those in states below nodes are diamagnetic^{6,7}. Weyl semimetals possess a magnetic field-independent 0th Landau level. As a field increases, Landau level splitting pushes higher Landau levels above Fermi level, and electrons are absorbed by the lower Landau levels. In this rearrangement, the 0th Landau level sustains its position. Therefore, it can accommodate more electrons with the help of increasing Landau level degeneracy by the magnetic field, resulting in a paramagnetic response. The paramagnetism rooted in a π Berry phase is referred to as the Berry paramagnetism. Since DSMs have a linear dispersion with a π Berry phase, similar to Weyl semimetals, we may apply the concept of the Berry paramagnetism. Moreover, ZrTe_5 is known to have a Dirac cone at Γ point and a small gap, which provides the justification. We simulated the magnetic data of our DSM of $\text{Ti}_x\text{Zr}_{1-x}\text{Te}_5$ using the Berry paramagnetism. Figure 5f shows the simulated curves (dashed lines) and the magnetization curve (solid line) measured at 2 K. We used the band parameters of v_a, v_b, v_c and E_F obtained from analyzing our results (Supplementary Note 4). It is noteworthy that there is only one fitting parameter of the g factor, $g = 10$, which is reasonable considering the previous results^{24,25,30}. Since the diamagnetic contribution is constant at temperatures below T_m , the magnetic response is mainly dominated by the Berry paramagnetism of the conduction band electrons. There are shown clear dHvA oscillations below the quantum limit (~ 7 T), while the paramagnetic contribution decreases above the quantum limit (Supplementary Note 6). As the Fermi level is lowered, the magnetic field for entering the quantum limit also decreases, leading to a smaller paramagnetic signal. Indeed, the simulated curves with $E_F = 20$ and 10 meV show smaller paramagnetic responses than those with $E_F = 31.85$ meV. Since a lower E_F value corresponds to an increased temperature, the decreasing magnetization with increasing temperature from 2 K to T_m in Fig. 5a is well explained. Moreover, as E_F decreases, a required magnetic field for the quantum limit decreases, but quantum oscillations are not visible because of thermal energy. Moreover, we explored the cases when a magnetic field is applied along the other directions, along with the a and c axes (Supplementary Note 7). The calculated magnetization curves for $H//a$ and $H//c$ are much smaller than those for $H//b$, which is in good agreement with our experimental data (see Fig. 5a). Finally, by adding a strong diamagnetic background from valence band electrons, we reproduced the magnetization data, verifying the Berry paramagnetism in ZrTe_5 (Supplementary Note 8). On the other hand, the increasing magnetization with increasing temperatures from T_m to 300 K is understandable considering a decreasing diamagnetic contribution of the valence band electrons (Supplementary Note 8). Since the diamagnetism from the valence band has the same mechanism as the Berry paramagnetism, it changes with a comparable magnitude with the Berry paramagnetism. As a result, the magnetization shows a minimum at T_m , where the E_F is located at the Dirac point, because the Berry paramagnetism is minimized and the total diamagnetic signal is maximized.

Conclusions

We successfully fabricated single crystals of $\text{Ti}_x\text{Zr}_{1-x}\text{Te}_5$, where Zr was substituted with Ti by a chemical vapor transport method, and observed systematic changes in transport and magnetic properties. Since Ti has a smaller atomic radius than Zr, the isovalent Ti substitution can finely tune the band structure due to the decrease in the

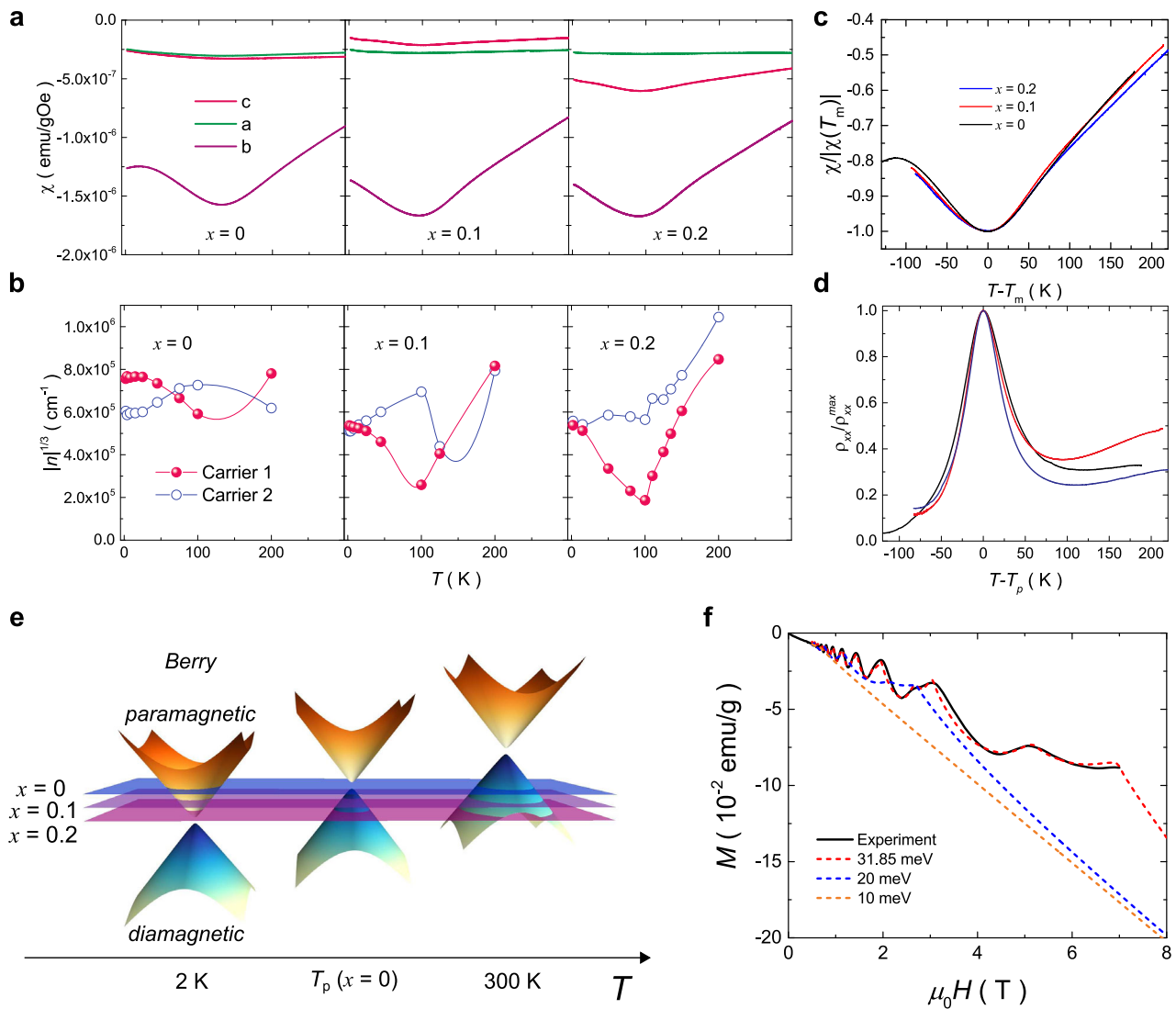


Fig. 5 Correlation between resistivity and susceptibility. **a** Temperature dependence of susceptibilities with 7 T of a magnetic field along with *a*, *b*, and *c* axes. **b** Temperature dependence of $|n|^{1/3}$ of carriers 1 and 2. The values of n were extracted from the two-carrier analyses. The error bars obtained using the standard error of the two-carrier fit to a power of $1/3$ are smaller than the size of the data symbols. **c** Normalized susceptibility curves. The susceptibilities were divided by the maximum value and plotted as a function of the relative temperature, $T - T_m$, where T_m is the temperature at which the susceptibility shows its minimum. **d** Normalized resistivity curves. The resistivities were divided by the maximum value and plotted as a function of the relative temperature, $T - T_p$, where T_p is the temperature at which the resistivity shows its peak. **e** Schematic picture for magnetic susceptibility and band shift depending on temperature for three samples. The planes show the Fermi energy of each sample at 2 K. **f** Simulated magnetization curves of $x = 0$ at 2 K for various Fermi energies. The solid black line denotes the experimental data, and the dashed lines represent simulated curves.

lattice constant. Quantum oscillation measurements indicate that the single crystals of $\text{Ti}_x\text{Zr}_{1-x}\text{Te}_5$ are 3D DSMs with anisotropic quasi-2D Fermi surface. The temperature dependence of quantum oscillation frequency supports the Lifshitz transition. Though we cannot rule out temperature-dependent gap opening, the estimated carrier density changes its sign, implying that the Lifshitz transition is dominant in our crystals. The resistivity peak shifts to lower temperatures with increasing x , which coincides with the shift of the susceptibility minimum. Considering that transport properties are mostly governed by carrier motion around Fermi energy, whereas a magnetization is a bulk property related to a total magnetic moment below Fermi energy, it is not common that the carriers contributing to the transport properties play an important role in the temperature-dependent susceptibility. We demonstrated that the nontrivial fermions in states above the Dirac node contribute to

paramagnetism, while those in states below the node are diamagnetic.

In addition, the observed susceptibility smoothly changes with temperature, sustaining a large magnitude. If a topological phase transition^{8,17} occurs in our sample, the Berry magnetism would be strongly suppressed because a Dirac cone of topological insulator only resides on surfaces, and the number of Dirac fermions would be much smaller. In addition, the magnetic susceptibility curves behave similarly for $x = 0, 0.1$, and 0.2 . These results support that the Berry paramagnetism comes from the bulk; therefore, we confirm that our $\text{Ti}_x\text{Zr}_{1-x}\text{Te}_5$ crystals are 3D DSMs. This work not only proposes an experimental way to determine the topological character of the band but also provides a platform to apply the concept of π Berry phase-related band topology to DSMs.

Methods

Material growth. Single crystals of $\text{Ti}_x\text{Zr}_{1-x}\text{Te}_5$ with nominal compositions of $x = 0, 0.1, \text{ and } 0.2$ were prepared using a chemical vapor transport method. The compositions measured by electron probe microanalyzer were 1% for $x = 0.1$ and 2% for $x = 0.2$.

All samples were grown under the same conditions in a single batch. High purity of Zr (99.99%) and Te (99.99%) elements were evacuated and sealed in a quartz ampoule. For Ti-substituted samples, we replaced 10% and 20% of Zr with Ti. The mixtures of Ti, Zr, and Te were placed at 500 °C for solid-state reaction to synthesize homogeneous source materials. The reacted powder source was then kept in a two-zone furnace with iodine as a transport agent. The temperature of the source zone was 520 and 450 °C for the sink zone. The growth was sustained for a month to obtain large single crystals.

Characterization of single crystals by XRD. The crystal structures of $\text{Ti}_x\text{Zr}_{1-x}\text{Te}_5$ were characterized by XRD (Bruker D8 Advance diffractometer with Cu light source). A shiny surface of single crystals was set to be the diffraction plane which was determined to be the layer of the orthorhombic layered structure with the space group *Cmcm*. All the measurement parameters were scanned and aligned to maximize the intensity, and then θ - 2θ scans were performed.

Transport measurements. The electrical resistivity and the Hall effect were measured by a standard four-probe method using a physical properties measurement system equipped with a Keithley 2635 source measure unit and a Keithley 2182 A nanovoltmeter. The typical length of the crystals was ~10 mm. The four-probe electrical contacts were made through a gold wire by soldering with indium.

Magnetic measurements. The magnetic properties of $\text{Ti}_x\text{Zr}_{1-x}\text{Te}_5$ were measured using a superconducting quantum interference device-vibrating sample magnetometer at temperatures ranging from 2 to 300 K and at applied magnetic fields up to 7 T.

Data availability

All data needed to evaluate the conclusions in the paper are present in the paper and/or the Supplementary Materials. Additional data related to this paper may be requested from the authors.

Received: 12 May 2021; Accepted: 26 November 2021;

Published online: 14 December 2021

References

- Chang, C.-Z. et al. Experimental observation of the quantum anomalous Hall effect in a magnetic topological insulator. *Science* **340**, 167–170 (2013).
- Li, Q. et al. Chiral magnetic effect in ZrTe_5 . *Nat. Phys.* **12**, 550–554 (2016).
- Chang, C.-Z. & Li, M. Quantum anomalous Hall effect in time-reversal-symmetry breaking topological insulators. *J. Phys.: Condens. Matter* **28**, 123002 (2016).
- Liang, T. et al. Anomalous Hall effect in ZrTe_5 . *Nat. Phys.* **14**, 451–455 (2018).
- Deng, Y. et al. Quantum anomalous Hall effect in intrinsic magnetic topological insulator MnBi_2Te_4 . *Science* **367**, 895–900 (2020).
- Moll, P. J. W. et al. Magnetic torque anomaly in the quantum limit of Weyl semimetals. *Nat. Commun.* **7**, 12492 (2016).
- Zhang, C.-L. et al. Non-saturating quantum magnetization in Weyl semimetal TaAs. *Nat. Commun.* **10**, 1028 (2019).
- Nair, N. L. et al. Thermodynamic signature of Dirac electrons across a possible topological transition in ZrTe_5 . *Phys. Rev. B* **97**, 041111 (2018).
- Weng, H., Dai, X. & Fang, Z. Transition-metal pentatelluride ZrTe_5 and HfTe_5 : a paradigm for large-gap quantum spin Hall insulators. *Phys. Rev. X* **4**, 1–8 (2014).
- Fan, Z., Liang, Q.-F., Chen, Y. B., Yao, S.-H. & Zhou, J. Transition between strong and weak topological insulator in ZrTe_5 and HfTe_5 . *Sci. Rep.* **7**, 45667 (2017).
- Mutch, J. et al. Evidence for a strain-tuned topological phase transition in ZrTe_5 . *Sci. Adv.* **5**, eaav9771 (2019).
- Konstantinova, T. et al. Photoinduced Dirac semimetal in ZrTe_5 . *npj Quantum Mater.* **5**, 80 (2020).
- Manzoni, G. et al. Evidence for a strong topological insulator phase in ZrTe_5 . *Phys. Rev. Lett.* **117**, 237601 (2016).
- Wu, R. et al. Evidence for topological edge states in a large energy gap near the step edges on the surface of ZrTe_5 . *Phys. Rev. X* **6**, 021017 (2016).
- Zhang, Y. et al. Electronic evidence of temperature-induced Lifshitz transition and topological nature in ZrTe_5 . *Nat. Commun.* **8**, 15512 (2017).
- Chi, H. et al. Lifshitz transition mediated electronic transport anomaly in bulk ZrTe_5 . *N. J. Phys.* **19**, 015005 (2017).
- Xu, B. et al. Temperature-driven topological phase transition and intermediate Dirac semimetal phase in ZrTe_5 . *Phys. Rev. Lett.* **121**, 187401 (2018).
- Shahi, P. et al. Bipolar conduction as the possible origin of the electronic transition in pentatellurides: metallic vs semiconducting behavior. *Phys. Rev. X* **8**, 021055 (2018).
- Moreschini, L. et al. Nature and topology of the low-energy states in ZrTe_5 . *Phys. Rev. B* **94**, 081101 (2016).
- Wang, W. et al. Evidence for layered quantized transport in Dirac semimetal ZrTe_5 . *Sci. Rep.* **8**, 5125 (2018).
- Lv, Y. Y. et al. Shubnikov-de Haas oscillations in bulk ZrTe_5 single crystals: evidence for a weak topological insulator. *Phys. Rev. B* **97**, 115137 (2018).
- Okada, S. et al. Negative evidences for charge/spin density wave in ZrTe_5 . *J. Phys. Soc. Jpn.* **51**, 460–467 (1982).
- Smontara, A., Biljaković, K., Miljak, M. & Sambongi, T. Thermal and magnetic measurements on ZrTe_5 . *Phys. B+C*. **143**, 267–269 (1986).
- Liu, Y. et al. Zeeman splitting and dynamical mass generation in Dirac semimetal ZrTe_5 . *Nat. Commun.* **7**, 12516 (2016).
- Wang, J. et al. Vanishing quantum oscillations in Dirac semimetal ZrTe_5 . *PNAS* **115**, 9145–9150 (2018).
- Liang, T. et al. Ultrahigh mobility and giant magnetoresistance in the Dirac semimetal Cd_3As_2 . *Nat. Mater.* **14**, 280–284 (2015).
- Sasama, Y. et al. Quantum oscillations in diamond field-effect transistors with a h-BN gate dielectric. *Phys. Rev. Mater.* **3**, 121601 (2019).
- Hu, J., Xu, S.-Y., Ni, N. & Mao, Z. Transport of topological semimetals. *Annu. Rev. Mater. Res.* **49**, 207–252 (2019).
- Wang, Z. et al. Highly mobile carriers in a candidate of quasi-two-dimensional topological semimetal AuTe_2Br . *APL Mater.* **7**, 101110 (2019).
- Chen, R. Y. et al. Magnetoinfrared spectroscopy of Landau levels and Zeeman splitting of three-dimensional massless Dirac fermions in ZrTe_5 . *Phys. Rev. B* **115**, 176404 (2015).

Acknowledgements

The authors thank S. Choi for the measurement of STM and S. Joo for the help on the transport measurement. This work was supported by the National Research Foundation of Korea (NRF) (Grant No. 2020R1A2C3008044) and by Samsung Electronics Co., Ltd.

Author contributions

M.-H.J. supervised the overall research; S.J. synthesized ZrTe_5 single crystals and performed the magnetotransport measurements, the magnetization measurements, transport analysis, and the simulation of the magnetizations; S.-E.L. gave suggestions of theoretical explanation; and M.-H.J. and S.J. wrote the paper with help from all other coauthors.

Competing interests

The authors declare no competing interests.

Additional information

Supplementary information The online version contains supplementary material available at <https://doi.org/10.1038/s42005-021-00773-3>.

Correspondence and requests for materials should be addressed to Myung-Hwa Jung.

Peer review information *Communications Physics* thanks the anonymous reviewers for their contribution to the peer review of this work. Peer reviewer reports are available

Reprints and permission information is available at <http://www.nature.com/reprints>

Publisher's note Springer Nature remains neutral with regard to jurisdictional claims in published maps and institutional affiliations.



Open Access This article is licensed under a Creative Commons Attribution 4.0 International License, which permits use, sharing, adaptation, distribution and reproduction in any medium or format, as long as you give appropriate credit to the original author(s) and the source, provide a link to the Creative Commons license, and indicate if changes were made. The images or other third party material in this article are included in the article's Creative Commons license, unless indicated otherwise in a credit line to the material. If material is not included in the article's Creative Commons license and your intended use is not permitted by statutory regulation or exceeds the permitted use, you will need to obtain permission directly from the copyright holder. To view a copy of this license, visit <http://creativecommons.org/licenses/by/4.0/>.

© The Author(s) 2021